*Article*

# Improving the Stability of Lithium Aluminum Germanium Phosphate with Lithium Metal by Interface Engineering

Yue Zhang [1], Hanshuo Liu [2,*], Zhong Xie [2], Wei Qu [2] and Jian Liu [1,*]

[1] School of Engineering, Faculty of Applied Science, University of British Columbia, 3333 University Way, Kelowna, BC V1V 1V7, Canada; yue.zhang@ubc.ca
[2] Energy, Mining and Environment Research Center, National Research Council Canada, 4250 Wesbrook Mall, Vancouver, BC V6T 1W5, Canada; zhong.xie@nrc-cnrc.gc.ca (Z.X.); wei.qu@nrc-cnrc.gc.ca (W.Q.)
* Correspondence: hanshuo.liu@nrc-cnrc.gc.ca (H.L.); jian.liu@ubc.ca (J.L.)

**Abstract:** Lithium aluminum germanium phosphate (LAGP) solid electrolyte is receiving increasing attention due to its high ionic conductivity and low air sensitivity. However, the poor interface compatibility between lithium (Li) metal and LAGP remains the main challenge in developing all-solid-state lithium batteries (ASSLB) with a long cycle life. Herein, this work introduces a thin aluminum oxide ($Al_2O_3$) film on the surface of the LAGP pellet as a physical barrier to Li/LAGP interface by the atomic layer deposition technique. It is found that this layer induces the formation of stable solid electrolyte interphase, which significantly improves the structural and electrochemical stability of LAGP toward metallic Li. As a result, the optimized symmetrical cell exhibits a long lifetime of 360 h with an areal capacity of 0.2 mAh $cm^{-2}$ and a current density of 0.2 mA $cm^{-2}$. This strategy provides new insights into the stabilization of the solid electrolyte/Li interface to boost the development of ASSLB.

**Keywords:** lithium aluminum germanium phosphate; lithium metal anode; interface modification; atomic layer deposition

## 1. Introduction

Lithium metal is a promising anode candidate for constructing high-energy-density lithium batteries due to its high specific capacity (3860 mAh $g^{-1}$) and low redox potential (−3.05 V vs. standard hydrogen electrode) [1,2]. Currently, its development is plagued by the intrinsic safety issues of liquid electrolytes because of the flammability of organic solvents used [3,4]. Replacing organic liquid electrolytes with non-flammable and highly conductive solid electrolytes (SEs) is an effective approach to improving battery safety [5,6]. With respect to this, there is growing research interest in the development of all-solid-state lithium-ion batteries (ASSLBs), and significant progress has been made over the past few years [7–9]. Critical characteristics of SEs include high lithium-ion conductivity, excellent chemical stability, and good mechanical properties [10]. Various SEs have been well developed, such as polymer-based SEs, garnet-type $Li_7La_3Zr_2O_{12}$ [11], sulfide [12], and NASICON-type $LiM_2(PO_4)_3$ (M = Ti, Ge, Hf, Zr, Sn) [13], as well as composite SEs [14–16]. Aluminum (Al) -doped NASICON-type $Li_{1+x}Al_xGe_{2-x}(PO_4)_3$ (LAGP) oxides have received tremendous attention due to their high chemical and electrochemical stability in the air, high ionic conductivity (>$10^{-4}$ S $cm^{-1}$), and good mechanical strength [10]. The fast Li-ion conduction in the LAGP system benefits from the main Li-ion diffusion pathway along 36*f* and $M_2$ interstitial sites resulting from $Al^{3+}$ to $Ge^{4+}$ substitution [17]. LAGP SEs have been synthesized by various routes, from melt-quenching [18], sintering [19], sol-gel [20], to hot-press [21], etc. Controlling key parameters such as crystallization and sintering temperature or pressure is critical in tailoring desirable highly-conductive LAGP pellets [21–23].

Li/LAGP interfacial incompatibility remains the main challenge for the further development of ASSLBs. Due to the high Fermi energy level of Li metal, germanium (Ge) in

LAGP would be irreversibly degraded upon being contacted with Li metal at the Li/LAGP interface, resulting in an increased impedance versus time [24]. When an electrical current is applied to the Li metal anode, part of Li ions can be reduced at the LAGP side, leading to a local volume expansion which triggers cracks in the LAGP SE [25]. These cracks could cause the pulverization of SEs, mechanical deterioration, or even cell failure (short circuit) [26]. Consequently, the unstable Li/LAGP interface causes inferior cell capacity and lifetime, which need to be mitigated using effective interfacial stabilization strategies.

Li et al. [27] introduced a succinonitrile-based plastic interlayer between Li metal and LAGP by in situ solidification. This interlayer isolated the direct contact between Li and LAGP and regulated uniform Li-ion distribution, which enabled a 240-h cycle life in symmetrical Li cells. Zhou et al. [28] sputtered an amorphous Ge thin film on the LAGP surface, which ensured intimate Li/LAGP contact and suppressed the unexpected Ge reduction, thus contributing to a superior symmetrical cell over 100 cycles at 0.1 mA cm$^{-2}$. Xiong et al. [29] created a quasi-solid-state paste interlayer composed of LAGP nanoparticles and ionic liquid, which enabled fast Li-ion conduction and improved chemical stability toward metallic Li, and suppressed thermal runaway. Sun et al. [30] adopted the atomic layer deposition (ALD) technique to coat ultrathin aluminum oxide ($Al_2O_3$) on the surface of $Li_{1.3}Al_{0.3}Ti_{1.7}(PO_4)_3$ (LATP), and the Li/LATP interface was significantly stabilized at 0.01 mA cm$^{-2}$. Currently, most Li/LAGP/Li symmetrical cells show a long cycle time at a low current density of 0.1 mA cm$^{-2}$ [1,3,25,26,28,31–37], making it hard to meet the demand for practical applications. Improving the electrochemical stability of LAGP at higher current densities is an urgent task in the development of high-energy-density ASSLBs [38].

In this work, the effect of sintering temperature on the structure and ionic conductivity of LAGP is investigated, and 850 °C is found as the optimal sintering temperature to reach an ionic conductivity of $2.4 \times 10^{-4}$ S cm$^{-1}$ at room temperature. Furthermore, an ultrathin $Al_2O_3$ coating layer is deposited in the LAGP pellet surface via the ALD technique, which physically isolates the contact between Li metal and LAGP SE and enhances the electrochemical stability of LAGP toward metallic Li. The Li symmetrical cell with $Al_2O_3$-coated LAGP SE showed an excellent lifetime of 360 h at a current density of 0.2 mA cm$^{-2}$ and capacity density of 0.2 mAh cm$^{-2}$, which is higher than most previously reported Li/LAGP/Li cells with interlayer modification.

## 2. Materials and Methods

### 2.1. Materials

LAGP powders with a stoichiometric formula of $Li_{1.5}Al_{0.5}Ge_{1.5}(PO_4)_3$ were purchased from the Shanghai Institute of Ceramics (Shanghai, China). The precursors for ALD were trimethylaluminium (TMA) and deionized water ($H_2O$). Lithium hexafluorophosphate ($LiPF_6$, Gotion, CAS: 21324-40-3), ethylene carbonate (EC, Gotion, CAS: 96-49-1), and diethyl carbonate (DEC, Gotion, CAS: 105-58-8) were used as received for coin cell assembly.

### 2.2. Preparation of LAGP Pellets

LAGP pellets were made by a conventional dry-pressing method (15T Compact Hydraulic Pellet Press, MTI Corporation, Richmond, CA, USA). To begin, 0.2 g LAGP of powder was placed into a stainless-steel die with 12 mm diameter and pressed at 200 MPa uniaxial pressure at room temperature for 2 min. The obtained pellets were then transferred into a ceramic crucible. The sintering process was conducted at 800–900 °C in the air for 6 h at a heating rate of 2° min$^{-1}$ in a tube furnace. The thickness of the as-prepared LAGP pellets was about 0.8 mm.

### 2.3. Atomic Layer Deposition of $Al_2O_3$ on LAGP

The $Al_2O_3$ layer was coated on LAGP in a commercial ALD reactor (GEMStar™ XT Atomic Layer Deposition Systems, Singapore). The coating process was carried out at 100 °C by following a TMA pulse/TMA purge/$H_2O$ pulse/$H_2O$ purge sequence in each cycle. After 50 cycles, $Al_2O_3$ films were deposited on LAGP noted as LAGP@$Al_2O_3$50.

### 2.4. Materials Characterizations

The morphologies and microstructures of LAGP powder and pallets were observed and analyzed by scanning electron microscopy (SEM) and energy dispersive spectroscopy (EDS). X-ray diffraction (XRD) was used to analyze the crystal structure of LAGP. Surface elemental analysis was investigated by X-ray photoelectron spectroscopy (XPS).

Electrochemical impedance spectroscopy EIS measurements were carried out at 25 °C and elevated temperatures (30–60 °C). The LAGP pellets were Au-coated on both sides as electrodes and clamped for conduction. The ionic conductivity ($\sigma$) of LAGP was measured by Equation (1):

$$\sigma = \frac{L}{RA} \tag{1}$$

where $L$ and $A$ are the thickness and effective area of LAGP, respectively, and $R$ is the resistance obtained by EIS) testing within a frequency range of $0.01$–$10^6$ Hz with an AC amplitude of 5 mV.

### 2.5. Electrochemical Measurements

CR2032 cells were assembled in an argon-filled glovebox workstation with $H_2O$ and $O_2$ less than 0.1 ppm. First, 10 μL electrolyte (1 M $LiPF_6$ in EC: DEC) were added to each Li/LAGP/Li cell. Symmetrical Li/LAGP/Li cells were tested in NEWARE battery cycler (CT-4008T-5V50mA-164, Shenzhen, China) at room temperature and 40 °C with current densities ranging from 0.02 to 0.2 mA cm$^{-2}$ with a plating-striping time of 1 h. The cycled Li/LAGP batteries were disassembled in the argon-filled glove box and then characterized by SEM and XPS to collect surface composition information.

## 3. Results and Discussion

Figure 1 presents the SEM images of LAGP pellets sintered at 800, 850, and 900 °C, respectively. Most LAGP particles have small sizes of less than 1 μm, as shown in Figure S1. After being pressed and sintered at high temperatures (800–900 °C), LAGP particles were closely stacked to form a dense surface, and no pores were found in higher-magnification images, ensuring continuous Li-ion pathways to achieve high ionic conductivity. The ionic conductivity of LAGP solid electrolyte relies on the Li-ion conduction in both bulk ($\sigma_{bulk}$) and along the grain boundary ($\sigma_{gb}$). With the sintering temperature increasing, unit cell volumes would grow to form wider Li-ion migration channels, thus leading to higher bulk conductivity $\sigma_{bulk}$ [23,39]. The Li-ion conduction along the grain boundary ($\sigma_{gb}$) mainly depends on grain-grain ceramics contact and density. High sintering temperatures above 850 °C would possibly induce cracks due to grain strain, decrease ceramics density, and slow down Li-ion transport at the grain boundary [23,40,41]. Consequently, LAGP sintered at 850 °C showed the highest ionic conductivity.

XRD patterns of LAGP pellets sintered at 800–900 °C are shown in Figure 2a. All the characteristic peaks of LAGP pellets match well with the LAGP powders and can be indexed as $LiGe_2(PO_4)_3$ (JCPDS PDF No. 80-1924). Figure 2b gives the Nyquist plot of LAGP pellets sintered at 800–900 °C measured in a frequency range of $0.01$–$1 \times 10^6$ Hz at room temperature. LAGP T850 possesses a smaller electrochemical impedance (283 Ω) than LAGP T800 (390 Ω) and T900 (392 Ω), thus leading to higher ionic conductivity of $2.4 \times 10^{-4}$ S cm$^{-1}$ (vs. $2.0 \times 10^{-4}$ and $1.8 \times 10^{-4}$ S cm$^{-1}$ for T800 and T900, respectively) as illustrated in Figure 2c. Further, the relationship between impedance and temperature for LAGP T850 is plotted in Figure 2d. It could be found that the impedance markedly decreases from 260 to 92 Ω with temperature increasing from 30 to 60 °C, corresponding to the ionic conductivity from $2.6 \times 10^{-4}$ to $7.3 \times 10^{-4}$ S cm$^{-1}$. LAGP T850 will be selected as a reference for further electrochemical stability tests with Li metal due to its highest ionic conductivity.
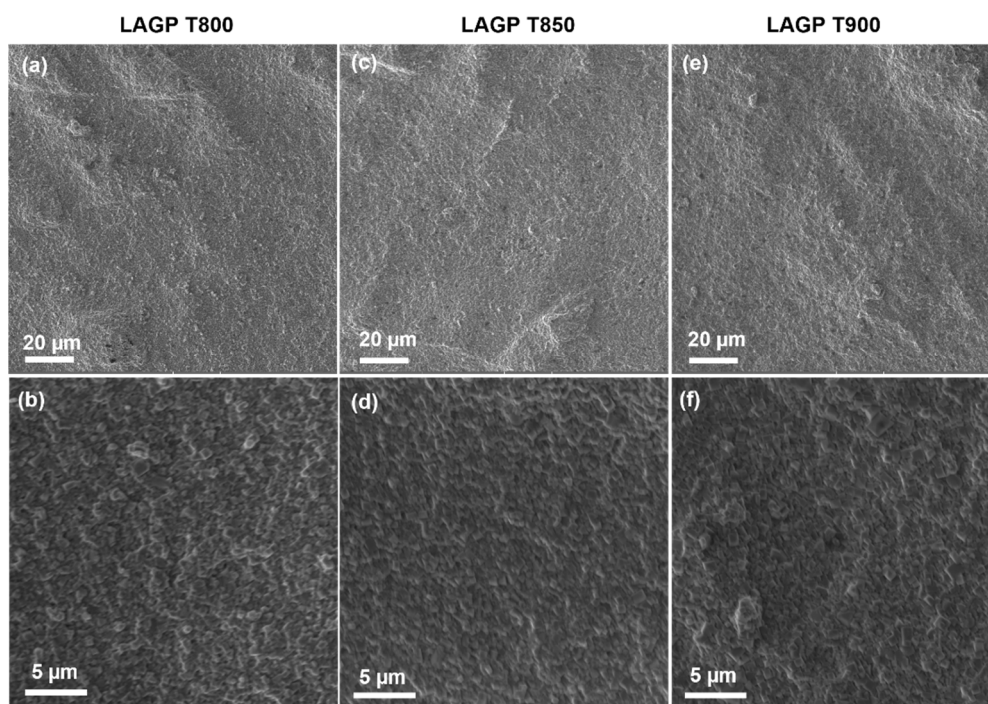
**Figure 1.** SEM images of LAGP pellets sintered at (**a**,**b**) 800 °C, (**c**,**d**) 850 °C, and (**e**,**f**) 900 °C.
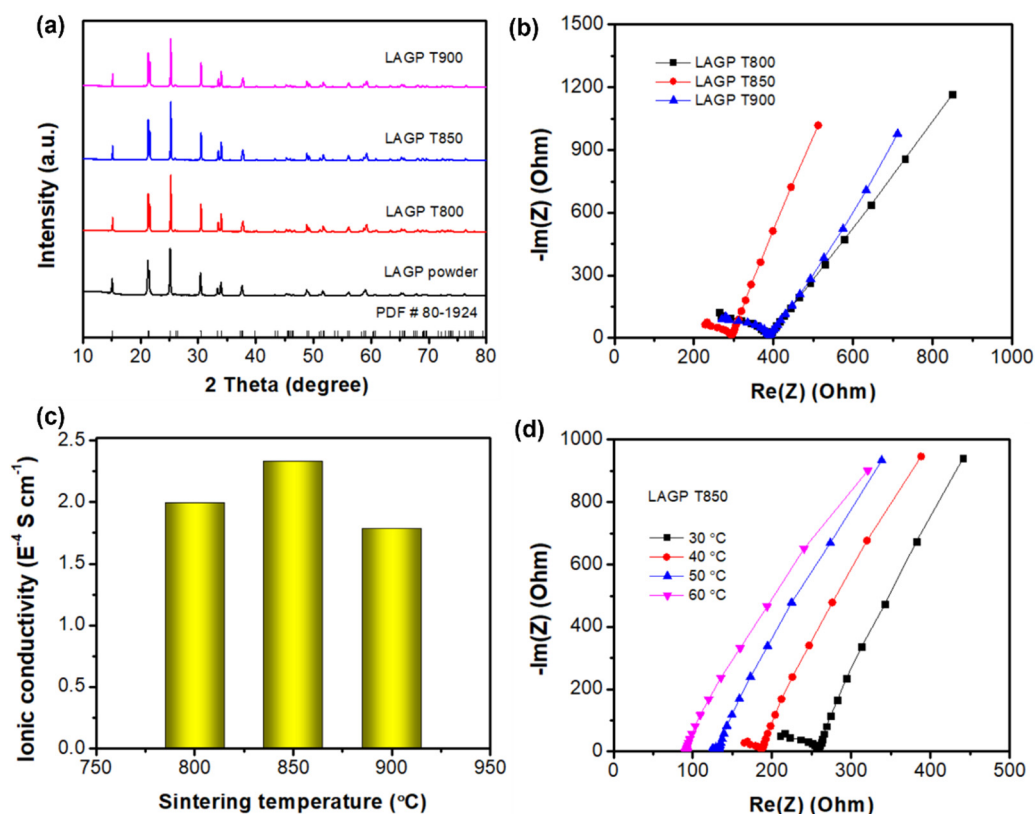


**Figure 2.** (**a**) XRD patterns, (**b**) Nyquist plots, (**c**) ionic conductivities of LAGP T800, LAGP T850, and LAGP T900 pellets, (**d**) Nyquist plots of LAGP T850 at 30–60 °C.

Figure S2 shows a voltage-time profile of Li/LAGP/Li symmetrical cell at room temperature. It could be found that the voltage hysteresis is gradually increasing at a low current density of 0.02 mA cm$^{-2}$ and rapidly rises to 3 V at only 0.04 mA cm$^{-2}$. The

large overpotential can be attributed to the unstable Li/LAGP interface and Li dendric deposition [26]. Herein, the $Al_2O_3$ layer is deposited on the surface of LAGP, as illustrated in Figure 3a, which can separate LAGP from the Li metal to prevent side reactions. The thickness of the $Al_2O_3$ layer is controlled at 5 nm based on our previous study on the P2-$Na_{0.66}(Mn_{0.54}Co_{0.13}Ni_{0.13})O_2$ cathode [42]. Figure 3b–g displays the SEM images of LAGP and LAGP@$Al_2O_3$50 from the top view and cross-section. Both demonstrate a compact and flat surface without pores. There is no noticeable change found in the surface and cross-section morphology.
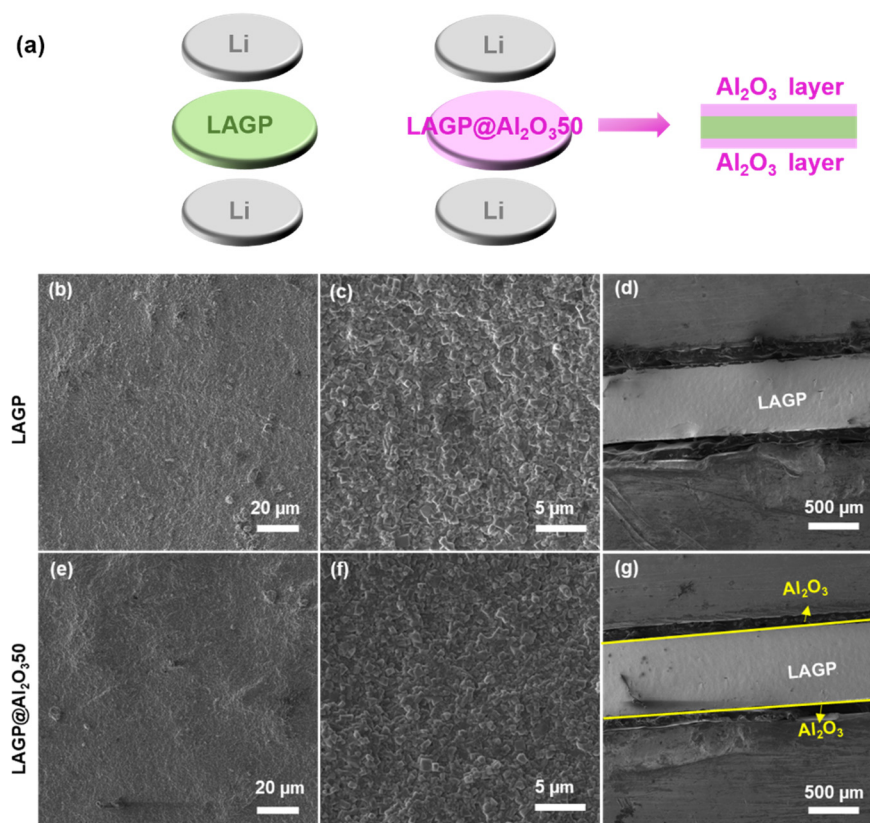


**Figure 3.** (**a**) Schematic illustration of Li/LAGP/Li and Li/LAGP@$Al_2O_3$/Li cell configurations, top-view and cross-sectional SEM images of (**b–d**) LAGP and (**e–g**) LAGP@$Al_2O_3$50.

XPS characterization was carried out to investigate the surface chemistry of LAGP with and without the $Al_2O_3$ layer. As shown in Figure S3 and Table S1, Ge, P, and Li elements are only detected on bare LAGP surface and absent for LAGP@$Al_2O_3$50, suggesting the successful deposition of $Al_2O_3$ film on the LAGP surface. The prominent peak in Li 1s XPS spectra (Figure 4a) is assigned to Li oxide of LAGP [43], while it is not detectable in LAGP@$Al_2O_3$50 (Figure 4b). Al 2p peaks can be resolved into $2p_{1/2}$ and $2p_{3/2}$ peaks corresponding to the existence of Al in LAGP and ALD-$Al_2O_3$ (Figure 4c,d). Similarly, P is only observed in bare LAGP (Figure 4e) and is absent for $Al_2O_3$-coated LAGP (Figure 4f). Therefore, it can be concluded that the thin $Al_2O_3$ layer by ALD is successfully deposited on the surface of LAGP without significant morphology change. The $Al_2O_3$ layer is expected to induce a stable interface between Li and LAGP, suppress side reactions, and enhance the electrochemical stability of LAGP toward metallic Li.

Figure 5a shows voltage profiles of symmetrical Li cells with bare and $Al_2O_3$-coated LAGP SEs at 0.02–0.2 mA cm$^{-2}$ at 40 °C. Li/LAGP/Li cell has a lower overpotential at the initial current density of 0.02 mA cm$^{-2}$, which becomes larger with the increase in current density and finally fails at 0.12 mA cm$^{-2}$. In comparison, the Li/LAGP@$Al_2O_3$50/Li cell exhibits a stable voltage hysteresis after initial cycles and undergoes a repeated Li

plating/stripping process at a much higher current density of 0.2 mA cm$^{-2}$. The steady voltage profiles of LAGP@Al$_2$O$_3$50 (Figure 5b,c) indicate the formation of a stable solid electrolyte interphase (SEI) between Li and LAGP. Long-term cycling performance is evaluated for the Li/LAGP@Al$_2$O$_3$50/Li cell, which exhibits a long lifetime of 320 h at the areal capacity of 0.2 mAh cm$^{-2}$ and current density of 0.2 mA cm$^{-2}$ (Figure 5d). The voltage hysteresis is mostly stabilized at 0.3 V until 250 h and then shows a slight increase, as illustrated in Figure 5e. It should be noted that the rate test is performed following the cycling test from the same Li/LAGP@Al$_2$O$_3$50/Li cell. Consequently, this cell has a 360-h Li plating/stripping duration at 0.2 mAh cm$^{-2}$.



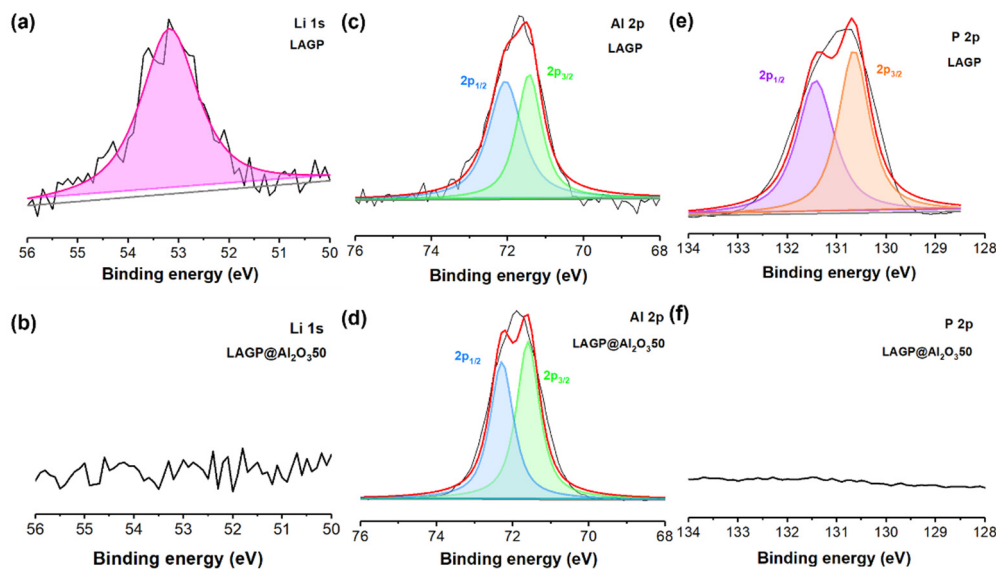**Figure 4.** XPS spectra of (**a**,**b**) Li 1s, (**c**,**d**) Al 2p, and (**e**,**f**) P 2p of LAGP and LAGP@Al$_2$O$_3$50.



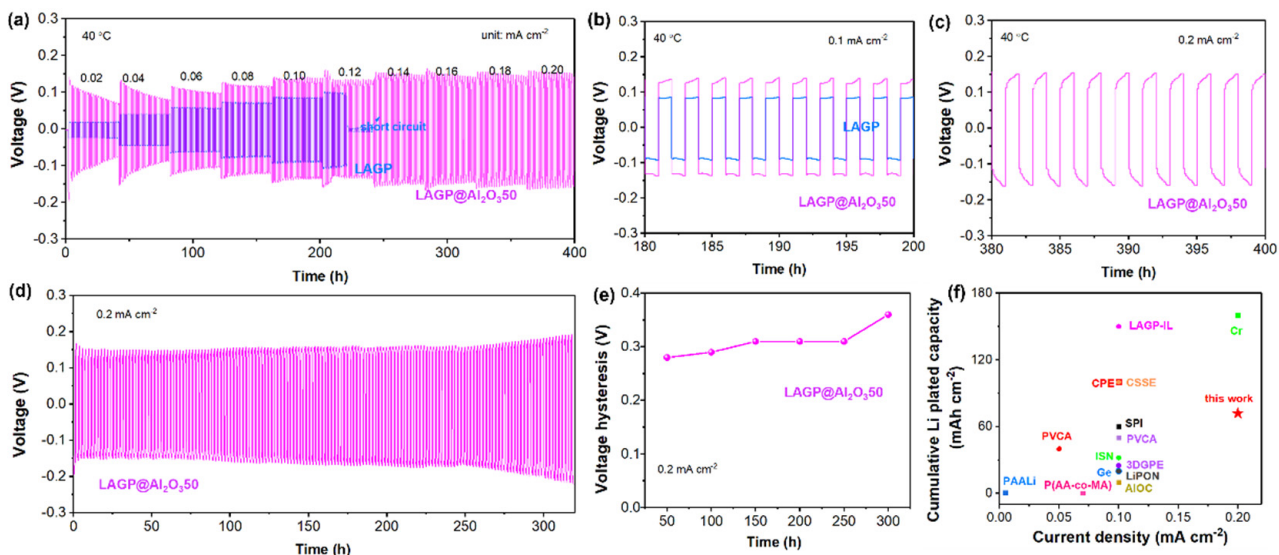**Figure 5.** (**a**) Rate performance of symmetrical Li cells with bare and Al$_2$O$_3$-coated LAGPs as SEs at 0.02–0.2 mA cm$^{-2}$ at 40 °C, voltage profiles at (**b**) 0.1 and (**c**) 0.2 mA cm$^{-2}$, (**d**) long-term cycling performance of the Li/LAGP@Al$_2$O$_3$50/Li cell at 0.2 mA cm$^{-2}$ (areal capacity: 0.2 mAh cm$^{-2}$) and (**e**) corresponding voltage hysteresis, (**f**) comparison of cumulative Li plated capacity from this work and literatures.

Moreover, Table 1 and Figure 5f compare cumulative Li plated capacity of previous Li/LAGP/Li cells and this work in the cycling test. It can be seen that most of the previous studies proposed polymer interlayer to modify Li/LAGP interface and assessed the cycling performance at 0.1 mA cm$^{-2}$, which demonstrated smaller cumulative Li plated capacity below 60 mAh cm$^{-2}$. Although the Li/Cr-LAGP-Cr/Li [3] cell showed a high Li plated capacity of 160 mAh cm$^{-2}$, the overpotential is as large as 1.2 V upon Li plating/stripping behaviors. In comparison, this work employs an inorganic Al$_2$O$_3$ layer to stabilize Li/LAGP interface, and the cell possesses a much smaller overpotential of 0.3 V at 0.2 mA cm$^{-2}$.

**Table 1.** Comparison of Li/LAGP/Li cells with interface modification.

| Cell Configuration | Interface Modification Layer | Cycling Performance | Cumulative Li Plated Capacity (mAh cm$^{-2}$) | References |
|---|---|---|---|---|
| Li/PP-LAGP-PP/Li * | PP | 500s @0.25 mA | - | [31] |
| Li/SPI-LAGP-SPI/Li * | SPI, by in situ solidification, 10 μm | 600 h @0.1 mA cm$^{-2}$ | 60 | [1] |
| PAALi/LAGP/PAALi * | PAALi + LAGP | 100 h @0.005 mA cm$^{-2}$ | 0.5 | [32] |
| Li/P(AA-co-MA)-LAGP-P(AA-co-MA)/Li | P(AA-co-MA), by spray-coating, 1.5 μm | 20,000 s @0.07 mA cm$^{-2}$ | 0.39 | [25] |
| Li/PVCA-LAGP-PVCA/Li * | LiTFSI/PVCA, | 500 h @0.1 mA cm$^{-2}$ | 50 | [33] |
| Li/AIOC-LAGP-AIOC/Li | AIOC, by spin coating, 11 μm | 100 h @0.1 mA cm$^{-2}$ | 10 | [34] |
| Li/CPE-LAGP-CPE/Li | CPE, by spin coating | 1000 h @0.1 mA cm$^{-2}$ | 100 | [36] |
| Li/lSN-LAGP-lSN/Li * | SN + LLZAO + FEC + LiTFSI, by in situ solidification | 320 h @0.1 mA cm$^{-2}$ | 32 | [27] |
| Li/Ge-LAGP-Ge/Li | Ge, by puttering, 60 nm | 200 h @0.1 mA cm$^{-2}$ | 20 | [28] |
| Li/Cr-LAGP-Cr/Li | Cr, by sputtering, 30 nm | 800 h @0.2 mA cm$^{-2}$ | 160 (overpotential: 1.2 V) | [3] |
| Li/LAGP-IL-LAGP-LAGP-IL/Li | LAGP-IL | 1500 h @0.1 mA cm$^{-2}$ | 150 | [29] |
| Li/3DGPE-LAGP-3DGPE/Li * | PVDF-HFP + PEGDE + DPPO, 100 μm | 250 h @0.1 mA cm$^{-2}$ | 25 | [44] |
| Li/CSSE-LAGP-CSSE/Li | PVC + TPU + LiTFSI, 50 μm | 1000 h @0.1 mA cm$^{-2}$ | 100 | [45] |
| Li/PVCA-LAGP-PVCA/Li | PVCA + FEC | 800 h @0.05 mA cm$^{-2}$ | 40 | [37] |
| Li/LiPON-LAGP-LiPON/Li | LiPON, by sputtering, 3 μm | 200 h @0.1 mA cm$^{-2}$ | 20 | [26] |
| Li/Al$_2$O$_3$-LAGP- Al$_2$O$_3$/Li * | Al$_2$O$_3$, by ALD, 5 nm | 360 h @0.2 mA cm$^{-2}$ | 72 (overpotential: 0.3 V) | This work |

*: 10 μL liquid electrolyte was used, or the interlayer was immersed in liquid electrolyte.

To reveal the internal structural change after repeated cycles, the cycled Li/LAGP/Li and Li/LAGP@Al$_2$O$_3$50/Li were disassembled for further analysis. Figure 6 shows the SEM images and digital photos of cycled LAGP and LAGP@Al$_2$O$_3$50. Abundant pores and cracks are observed in cycled-bare LAGP at different magnifications, and the cycled LAGP surface turns yellow, implying possible Ge$^{4+}$ reduction after being in contact with Li metal [25]. The pores and cracks may originate from continuous Li dendrite deposition at the unstable Li/LAGP interface and ultimately cause a short circuit failure [25,26]. On the contrary, Al$_2$O$_3$-coated LAGP illustrates a flat and dense surface after cycling, indicating the generation of stable SEI. This Al$_2$O$_3$-induced SEI regulates Li dendrites and induces a reliable symmetrical Li cell. Therefore, the deposited thin Al$_2$O$_3$ film is beneficial for stabilizing the Li/LAGP interface and regulating Li dendrites.
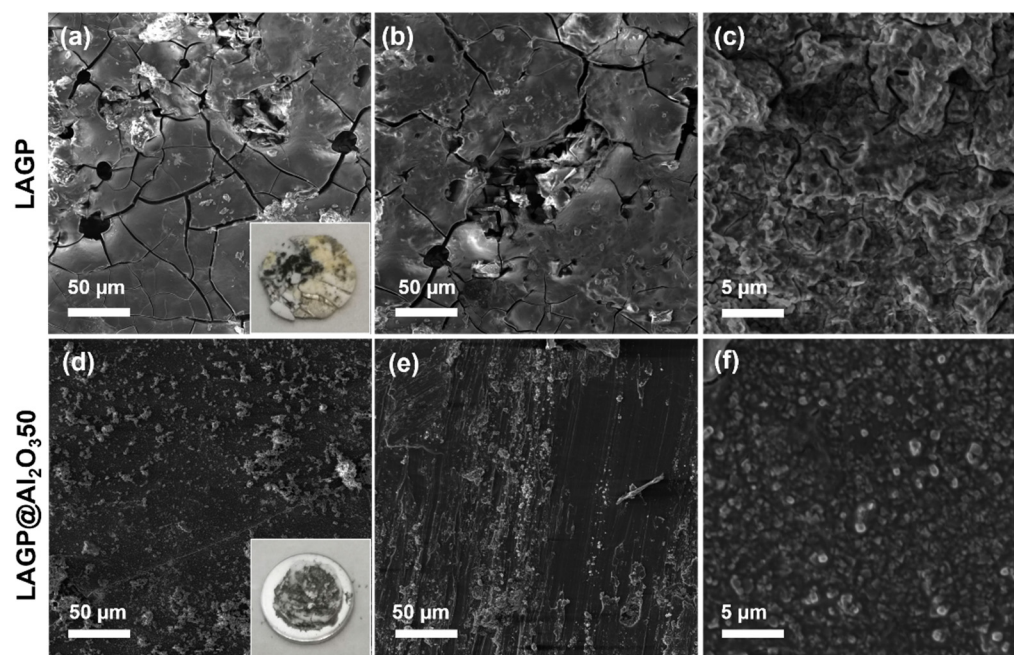
**Figure 6.** Top-view SEM images of cycled (**a**–**c**) LAGP and (**d**–**f**) LAGP@Al$_2$O$_3$50. The insets of (**a,d**) show the photos of cycled LAGP and LAGP@Al$_2$O$_3$50.

Meanwhile, a XPS test was performed to collect surface elemental information of cycled LAGP and LAGP@Al$_2$O$_3$50. As shown in Figures S4 and 7a, and Table S2, the Al signal is absent in bare LAGP, implying the formation of an Al-deficient SEI layer. Al 2p spectra in Figure 7b can be assigned to two peaks at 72.2 and 71.5 eV, respectively, which slightly shift to 72.7 and 72.0 eV with 1060 s etching (corresponding to about 8.8 nm depth from the top of the surface). Since the SEI layers are usually ~70 nm or thicker [46,47], both the 0 s and 1060 s etching spectra should come from the SEI layer instead of the LAGP SE. Meanwhile, the absence of Al signal from the cycled bare LAGP sample also indicates that the 1060 s etching does not reach the bulk LAGP SE. The peak shift of Al 2p spectra reveals the compositional variation in the SEI layer along the vertical direction of cycled LAGP@Al$_2$O$_3$50. The surface Li 1s spectrum (0 s etching) of cycled bare LAGP (Figure 7c) can be decomposed into two peaks located at 53.1 and 52.3 eV, respectively, corresponding to LiF and Li$_2$O$_2$ in the SEI layer. The surface Li 1s spectrum (0 s etching) obtained from LAGP@Al$_2$O$_3$50 shows higher binding energies of 53.5 and 53.0 eV for LiF and Li$_2$O$_2$ (Figure 7d). It should be noted that the Li 1s spectrum from cycled LAGP@Al$_2$O$_3$50 surface has a smaller LiF/Li$_2$O$_2$ ratio than cycled bare LAGP, suggesting the different SEI compositions from the coated and uncoated LAGPs. A higher LiF/Li$_2$O$_2$ ratio is observed in the Li 1s spectrum of cycled LAGP@Al$_2$O$_3$50 after 1060 s etching, implying a gradient distribution of LiF/Li$_2$O$_2$ in the SEI layer. F 1s spectra in Figure 7e,f originate from Li$_x$PF$_y$ and LiF, which could be ascribed to the decomposition of the small addition of liquid electrolyte (LiPF$_6$ in EC:DEC) [37]. The LiF/Li$_x$PF$_y$ ratio becomes larger for the LAGP@Al$_2$O$_3$50 after 1060s etching, which also indicates the compositional variation in the SEI layer along with the depth. The XPS results suggest that the SEI layers formed on the bared LAGP and Al$_2$O$_3$ coated LAGP possess different compositions. The Al$_2$O$_3$ coating induces an Al-containing SEI layer [48,49], formed on the surface of LAGP after repeated Li plating/stripping cycles. This unique SEI layer enhances the electrochemical stability of LAGP SE and extends the lifetime of Li/LAGP/Li symmetrical cells.
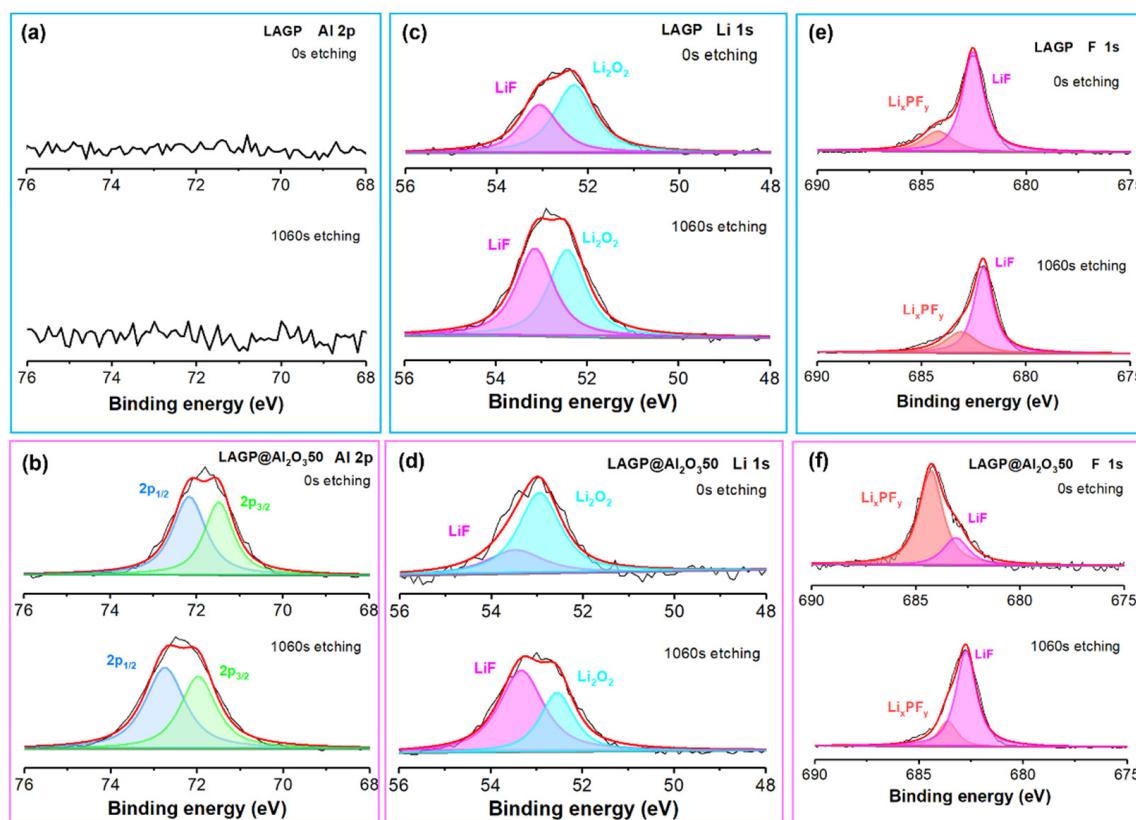
**Figure 7.** XPS spectra of (**a**,**b**) Al 2p, (**c**,**d**) Li 1s, (**e**,**f**) F 1s of the surface of LAGP and LAGP@Al$_2$O$_3$50 after cycling test.

## 4. Conclusions

In summary, a thin Al$_2$O$_3$ film was deposited on the surface of LAGP pellet by the ALD method to address the issue of Li/LAGP interface incompatibility. The optimized Li/LAGP@Al$_2$O$_3$50/Li cell maintained a stable voltage profile up to 0.2 mA cm$^{-2}$ and exhibited a 360-h cycling duration at the capacity density of 0.2 mAh cm$^{-2}$. Remarkably, this cell showed a superior cumulative Li plated capacity of 72 mAh cm$^{-2}$ at 0.2 mA cm$^{-2}$ current density. SEM and XPS characterizations suggest that Al$_2$O$_3$ film induced the formation of an Al-rich SEI layer to regulate Li dendrite deposition and contributes to a uniform and dense interface after long Li plating/stripping cycles.

**Supplementary Materials:** The following supporting information can be downloaded at: https://www.mdpi.com/article/10.3390/nano12111912/s1. Figure S1: SEM image of LAGP powder, Figure S2: Voltage-time profile of the Li/LAGP/Li cell tested at 25 °C, Figure S3: XPS survey spectra of LAGP and LAGP@Al$_2$O$_3$ before the cycling test, Figure S4: XPS survey spectra of LAGP and LAGP@Al$_2$O$_3$ after the cycling test, Table S1: Elemental composition of LAGP and LAGP@Al$_2$O$_3$50 from XPS before battery tests, Table S2: Elemental composition of LAGP and LAGP@Al$_2$O$_3$50 from XPS after cycling tests.

**Author Contributions:** Conceptualization, J.L. and H.L.; methodology, Y.Z. and J.L.; validation, Y.Z.; investigation, Y.Z. and H.L.; resources, J.L.; writing—original draft preparation, Y.Z.; writing—review and editing, Z.X., W.Q. and J.L.; visualization, Y.Z.; supervision, J.L.; funding acquisition, H.L. and J.L. All authors have read and agreed to the published version of the manuscript.

**Institutional Review Board Statement:** Not applicable.

**Informed Consent Statement:** Not applicable.

**Data Availability Statement:** Data is contained within the article or supplementary material.

**Conflicts of Interest:** The authors declare no conflict of interest.

## References

1. Cheng, Z.; Pan, H.; Li, C.; Mu, X.; Du, Y.; Zhang, F.; Zhang, X.; He, P.; Zhou, H. An in situ solidifying strategy enabling high-voltage all-solid-state Li-metal batteries operating at room temperature. *J. Mater. Chem. A* **2020**, *8*, 25217–25225. [CrossRef]
2. Han, X.; Chen, J.; Chen, M.; Zhou, W.; Zhou, X.; Wang, G.; Wong, C.P.; Liu, B.; Luo, L.; Chen, S.; et al. Induction of planar Li growth with designed interphases for dendrite-free Li metal anodes. *Energy Storage Mater.* **2021**, *39*, 250–258. [CrossRef]
3. Cortes, F.J.Q.; Lewis, J.A.; Tippens, J.; Marchese, T.S.; McDowell, M.T. How Metallic Protection Layers Extend the Lifetime of NASICON-Based Solid-State Lithium Batteries. *J. Electrochem. Soc.* **2019**, *167*, 050502. [CrossRef]
4. Gao, Z.; Sun, H.; Fu, L.; Ye, F.; Zhang, Y.; Luo, W.; Huang, Y. Promises, Challenges, and Recent Progress of Inorganic Solid-State Electrolytes for All-Solid-State Lithium Batteries. *Adv. Mater.* **2018**, *30*, e1705702. [CrossRef]
5. Manthiram, A.; Yu, X.; Wang, S. Lithium battery chemistries enabled by solid-state electrolytes. *Nat. Rev. Mater.* **2017**, *2*, 16103. [CrossRef]
6. Sun, C.; Liu, J.; Gong, Y.; Wilkinson, D.P.; Zhang, J. Recent advances in all-solid-state rechargeable lithium batteries. *Nano Energy* **2017**, *33*, 363–386. [CrossRef]
7. Zheng, F.; Kotobuki, M.; Song, S.; Lai, M.O.; Lu, L. Review on solid electrolytes for all-solid-state lithium-ion batteries. *J. Power Sources* **2018**, *389*, 198–213. [CrossRef]
8. Wang, Q.; Jiang, L.; Yu, Y.; Sun, J. Progress of enhancing the safety of lithium ion battery from the electrolyte aspect. *Nano Energy* **2019**, *55*, 93–114. [CrossRef]
9. Chen, J.; Wu, J.; Wang, X.; Zhou, A.A.; Yang, Z. Research progress and application prospect of solid-state electrolytes in commercial lithium-ion power batteries. *Energy Storage Mater.* **2021**, *35*, 70–87. [CrossRef]
10. Ye, T.; Li, L.; Zhang, Y. Recent Progress in Solid Electrolytes for Energy Storage Devices. *Adv. Funct. Mater.* **2020**, *30*, 2000077. [CrossRef]
11. Lu, W.; Xue, M.; Zhang, C. Modified $Li_7La_3Zr_2O_{12}$ (LLZO) and LLZO-polymer composites for solid-state lithium batteries. *Energy Storage Mater.* **2021**, *39*, 108–129. [CrossRef]
12. Chen, S.; Xie, D.; Liu, G.; Mwizerwa, J.P.; Zhang, Q.; Zhao, Y.; Xu, X.; Yao, X. Sulfide solid electrolytes for all-solid-state lithium batteries: Structure, conductivity, stability and application. *Energy Storage Mater.* **2018**, *14*, 58–74. [CrossRef]
13. Hou, M.; Liang, F.; Chen, K.; Dai, Y.; Xue, D. Challenges and perspectives of NASICON-type solid electrolytes for all-solid-state lithium batteries. *Nanotechnology* **2020**, *31*, 132003. [CrossRef] [PubMed]
14. Liu, Y.; He, P.; Zhou, H. Rechargeable Solid-State Li-Air and Li-S Batteries: Materials, Construction, and Challenges. *Adv. Energy Mater.* **2018**, *8*, 1701602. [CrossRef]
15. Li, L.; Deng, Y.; Chen, G. Status and prospect of garnet/polymer solid composite electrolytes for all-solid-state lithium batteries. *J. Energy Chem.* **2020**, *50*, 154–177. [CrossRef]
16. Li, S.; Zhang, S.-Q.; Shen, L.; Liu, Q.; Ma, J.-B.; Lv, W.; He, Y.-B.; Yang, Q.-H. Progress and Perspective of Ceramic/Polymer Composite Solid Electrolytes for Lithium Batteries. *Adv. Sci.* **2020**, *7*, 1903088. [CrossRef]
17. Kuo, P.H.; Du, J. Lithium Ion Diffusion Mechanism and Associated Defect Behaviors in Crystalline $Li_{1+x}Al_xGe_{2-x}(PO_4)_3$ Solid-State Electrolytes. *J. Phys. Chem. C* **2019**, *123*, 27385–27398. [CrossRef]
18. Yan, B.; Zhu, Y.; Pan, F.; Liu, J.; Lu, L. $Li_{1.5}Al_{0.5}Ge_{1.5}(PO_4)_3$ Li-ion conductor prepared by melt-quench and low temperature pressing. *Solid State Ion.* **2015**, *278*, 65–68. [CrossRef]
19. Yang, G.; Safanama, D.; Phuah, K.C.; Adams, S. Enhanced $Li_{1+x}Al_xGe_{2-x}(PO_4)_3$ Anode-Protecting Membranes for Hybrid Lithium-Air Batteries by Spark Plasma Sintering. *ACS Omega* **2020**, *5*, 18205–18212. [CrossRef]
20. Zhang, M.; Takahashi, K.; Imanishi, N.; Takeda, Y.; Yamamoto, O.; Chi, B.; Pu, J.; Li, J. Preparation and Electrochemical Properties of $Li_{1+x}Al_xGe_{2-x}(PO_4)$ Synthesized by a Sol-Gel Method. *J. Electrochem. Soc.* **2012**, *159*, A1114–A1119. [CrossRef]
21. Paolella, A.; Zhu, W.; Bertoni, G.; Perea, A.; Demers, H.; Savoie, S.; Girard, G.; Delaporte, N.; Guerfi, A.; Rumpel, M.; et al. Toward an All-Ceramic Cathode–Electrolyte Interface with Low-Temperature Pressed NASICON $Li_{1.5}Al_{0.5}Ge_{1.5}(PO_4)_3$ Electrolyte. *Adv. Mater. Inter.* **2020**, *7*, 2000164. [CrossRef]
22. Thokchom, J.S.; Kumar, B. The effects of crystallization parameters on the ionic conductivity of a lithium aluminum germanium phosphate glass–ceramic. *J. Power Sources* **2010**, *195*, 2870–2876. [CrossRef]
23. Pershina, S.V.; Pankratov, A.A.; Vovkotrub, E.G.; Antonov, B.D. Promising high-conductivity $Li_{1.5}Al_{0.5}Ge_{1.5}(PO_4)_3$ solid electrolytes: The effect of crystallization temperature on the microstructure and transport properties. *Ionics* **2019**, *25*, 4713–4725. [CrossRef]
24. Chung, H.; Kang, B. Mechanical and Thermal Failure Induced by Contact between a $Li_{1.5}Al_{0.5}Ge_{1.5}(PO_4)_3$ Solid Electrolyte and Li Metal in an All Solid-State Li Cell. *Chem. Mater.* **2017**, *29*, 8611–8619. [CrossRef]

25. He, L.; Sun, Q.; Chen, C.; Oh, J.A.S.; Sun, J.; Li, M.; Tu, W.; Zhou, H.; Zeng, K.; Lu, L. Failure Mechanism and Interface Engineering for NASICON-Structured All-Solid-State Lithium Metal Batteries. *ACS Appl. Mater. Interfaces* **2019**, *11*, 20895–20904. [CrossRef] [PubMed]

26. Zhang, Z.; Chen, S.; Yang, J.; Liu, G.; Yao, X.; Cui, P.; Xu, X. Stable cycling of all-solid-state lithium battery with surface amorphized $Li_{1.5}Al_{0.5}Ge_{1.5}(PO_4)_3$ electrolyte and lithium anode. *Electrochim. Acta* **2019**, *297*, 281–287. [CrossRef]

27. Liu, Q.; Yu, Q.; Li, S.; Wang, S.; Zhang, L.; Cai, B.; Zhou, D.; Li, B. Safe LAGP-based all solid-state Li metal batteries with plastic super-conductive interlayer enabled by in-situ solidification. *Energy Storage Mater.* **2020**, *25*, 613–620. [CrossRef]

28. Liu, Y.; Li, C.; Li, B.; Song, H.; Cheng, Z.; Chen, M.; He, P.; Zhou, H. Germanium Thin Film Protected Lithium Aluminum Germanium Phosphate for Solid-State Li Batteries. *Adv. Energy Mater.* **2018**, *8*, 1702374. [CrossRef]

29. Xiong, S.; Liu, Y.; Jankowski, P.; Liu, Q.; Nitze, F.; Xie, K.; Song, J.; Matic, A. Design of a Multifunctional Interlayer for NASCION-Based Solid-State Li Metal Batteries. *Adv. Funct. Mater.* **2020**, *30*, 2001444. [CrossRef]

30. Liu, Y.; Sun, Q.; Zhao, Y.; Wang, B.; Kaghazchi, P.; Adair, K.R.; Li, R.; Zhang, C.; Liu, J.; Kuo, L.-Y.; et al. Stabilizing the Interface of NASICON Solid Electrolyte against Li Metal with Atomic Layer Deposition. *ACS Appl. Mater. Interfaces* **2018**, *10*, 31240–31248. [CrossRef]

31. Bosubabu, D.; Sivaraj, J.; Sampathkumar, R.; Ramesha, K. LAGP|Li Interface Modification through a Wetted Polypropylene Interlayer for Solid State Li-Ion and Li–S batteries. *ACS Appl. Energy Mater.* **2019**, *2*, 4118–4125. [CrossRef]

32. He, L.; Chen, C.; Kotobuki, M.; Zheng, F.; Zhou, H.; Lu, L. A new approach for synthesizing bulk-type all-solid-state lithium-ion batteries. *J. Mater. Chem. A* **2019**, *7*, 9748–9760. [CrossRef]

33. Hu, Y.; Zhong, Y.; Qi, L.; Wang, H. Inorganic/polymer hybrid layer stabilizing anode/electrolyte interfaces in solid-state Li metal batteries. *Nano Res.* **2020**, *13*, 3230–3234. [CrossRef]

34. Li, C.; Chen, Y.; Li, Z.; Zhang, Y.; Fang, Z.; Xu, J.; Sun, Y.; Bao, H.; Cheng, H. Construction of sticky ionic conductive buffer layer for inorganic electrolyte toward stable all-solid-state lithium metal batteries. *J. Power Sources* **2021**, *495*, 229765. [CrossRef]

35. Li, L.; Zhang, Z.; Luo, L.; You, R.; Jiao, J.; Huang, W.; Wang, J.; Li, C.; Han, X.; Chen, S. Enhancing the interface stability of $Li_{1.3}Al_{0.3}Ti_{1.7}(PO_4)_3$ and lithium metal by amorphous $Li_{1.5}Al_{0.5}Ge_{1.5}(PO_4)_3$ modification. *Ionics* **2020**, *26*, 3815–3821. [CrossRef]

36. Li, W.; Wang, Q.; Jin, J.; Li, Y.; Wu, M.; Wen, Z. Constructing dual interfacial modification by synergetic electronic and ionic conductors: Toward high-performance LAGP-Based Li-S batteries. *Energy Storage Mater.* **2019**, *23*, 299–305. [CrossRef]

37. Zhang, S.; Zeng, Z.; Zhai, W.; Hou, G.; Chen, L.; Ci, L. Bifunctional In Situ Polymerized Interface for Stable LAGP-Based Lithium Metal Batteries. *Adv. Mater. Inter.* **2021**, *8*, 2100072. [CrossRef]

38. Kerman, K.; Luntz, A.; Viswanathan, V.; Chiang, Y.-M.; Chen, Z. Review—Practical Challenges Hindering the Development of Solid State Li Ion Batteries. *J. Electrochem. Soc.* **2017**, *164*, A1731–A1744. [CrossRef]

39. Zhu, Y.; Zhang, Y.; Lu, L. Influence of crystallization temperature on ionic conductivity of lithium aluminum germanium phosphate glass-ceramic. *J. Power Sources* **2015**, *290*, 123–129. [CrossRef]

40. DeWees, R.; Wang, H. Synthesis and Properties of NaSICON-type LATP and LAGP Solid Electrolytes. *ChemSusChem* **2019**, *12*, 3713–3725. [CrossRef]

41. Mariappan, C.R.; Yada, C.; Rosciano, F.; Roling, B. Correlation between micro-structural properties and ionic conductivity of $Li_{1.5}Al_{0.5}Ge_{1.5}(PO_4)_3$ ceramics. *J. Power Sources* **2011**, *196*, 6456–6464. [CrossRef]

42. Kaliyappan, K.; Liu, J.; Xiao, B.; Lushington, A.; Li, R.; Sham, T.-K.; Sun, X. Enhanced Performance of P2-$Na_{0.66}(Mn_{0.54}Co_{0.13}Ni_{0.13})O_2$ Cathode for Sodium-Ion Batteries by Ultrathin Metal Oxide Coatings via Atomic Layer Deposition. *Adv. Funct. Mater.* **2017**, *27*, 1701870. [CrossRef]

43. Oswald, S.; Thoss, F.; Zier, M.; Hoffmann, M.; Jaumann, T.; Herklotz, M.; Nikolowski, K.; Scheiba, F.; Kohl, M.; Giebeler, L.; et al. Binding Energy Referencing for XPS in Alkali Metal-Based Battery Materials Research (II): Application to Complex Composite Electrodes. *Batteries* **2018**, *4*, 36. [CrossRef]

44. Yu, Q.; Han, D.; Lu, Q.; He, Y.-B.; Li, S.; Liu, Q.; Han, C.; Kang, F.; Li, B. Constructing Effective Interfaces for $Li_{1.5}Al_{0.5}Ge_{1.5}(PO_4)_3$ Pellets To Achieve Room-Temperature Hybrid Solid-State Lithium Metal Batteries. *ACS Appl. Mater. Interfaces* **2019**, *11*, 9911–9918. [CrossRef]

45. Zhai, P.; Fu, L.; Yuan, S.; Shi, L.; Zhu, J.; Zhao, Y.; Wang, Z. Ionic Conductive Thermoplastic Polymer Welding Layer for Low Electrode/Solid Electrolyte Interface Resistance. *ACS Appl. Energy Mater.* **2020**, *3*, 7011–7019. [CrossRef]

46. Wang, M.; Huai, L.; Hu, G.; Yang, S.; Ren, F.; Wang, S.; Zhang, Z.; Chen, Z.; Peng, Z.; Shen, C.; et al. Effect of LiFSI Concentrations To Form Thickness- and Modulus-Controlled SEI Layers on Lithium Metal Anodes. *J. Phys. Chem. C* **2018**, *122*, 9825–9834. [CrossRef]

47. Nojabaee, M.; Kuster, K.; Starke, U.; Popovic, J.; Maier, J. Solid Electrolyte Interphase Evolution on Lithium Metal in Contact with Glyme-Based Electrolytes. *Small* **2020**, *16*, e2000756. [CrossRef]

48. Jung, S.C.; Han, Y.-K. How Do Li Atoms Pass through the $Al_2O_3$ Coating Layer during Lithiation in Li-ion Batteries? *J. Phys. Chem. Lett.* **2013**, *4*, 2681–2685. [CrossRef]

49. Zhang, B.; Zhong, J.; Pan, F.; Lin, Z. Potential Solid-State Electrolytes with Good Balance between Ionic Conductivity and Electrochemical Stability: $Li_{5-x}M_{1-x}M_x'O_4$ (M = Al and Ga and M′ = Si and Ge). *ACS Appl. Mater. Interfaces* **2021**, *13*, 61296–61304. [CrossRef]